Ground-state phase diagram of the three-band Hubbard model in various parametrizations from density matrix embedding theory

Zhi-Hao Cui,[1] Chong Sun,[1] Ushnish Ray,[1] Bo-Xiao Zheng,[2,1,3] Qiming Sun,[4,1] and Garnet Kin-Lic Chan[1,*]

[1]*Division of Chemistry and Chemical Engineering, California Institute of Technology, Pasadena, California 91125, United States*
[2]*AxiomQuant Investment Management LLC, Shanghai 200120, China*
[3]*Department of Chemistry, Princeton University, New Jersey 08544, United States*
[4]*Tencent America LLC, Palo Alto, California 94306, United States*

(Dated: January 15, 2020)

We compute the ground-state phase diagram of the three-band Hubbard model in various published parametrizations using density matrix embedding theory. We study the atomic-scale nature of the antiferromagnetic (AF) and superconducting (SC) orders, explicitly including the oxygen degrees of freedom. In the case of the AF order, as expected, the local magnetic moment localizes entirely at the copper sites and decays with doping, while in the SC phase we observe a local $p_{x(y)}$ [or $d_{xz(yz)}$]-symmetry modulation of the pair density on the Cu-O bonds within the larger scale $d_{x^2-y^2}$-wave SC pairing order between Cu-Cu and O-O. While all parametrizations of the model display AF and SC phases, the decay of AF order with doping is too slow compared to the experimental phase diagram, and further, coexistence of AF and SC orders occurs in all parameter sets. Our work highlights the importance of the oxygen degrees of freedom in the study of atomic-scale SC orders, as well as the necessity of re-evaluating current parametrizations of the three-band Hubbard model.

I. INTRODUCTION

The three-band Hubbard model, also known as the Emery model [1], is generally believed to contain the essential physics of the high T_c cuprates that arises from the interplay between the copper $d_{x^2-y^2}$ and oxygen $p_{x(y)}$ orbitals in the CuO_2 layers. Given the complexity of the model, commonly, the three-band model is further simplified and several simpler low-energy Hamiltonians have been proposed, such as the one-band Hubbard model [2, 3], t-J model [3, 4], and two-band model [5]. The first two are effective one-band models and are equivalent in the strong-coupling limit. In particular, the 2D one-band Hubbard model has been extensively investigated using various numerical approaches (see Ref. [6, 7] and the references therein). Much of the physics seen in high T_c materials, e.g. d-wave pairing, density waves, the pseudogap phase and stripe order, has been observed in studies of the simple one-band Hubbard within certain ranges of parameters [7].

However, despite the progress in understanding the one-band Hubbard model and its variants, there are still important reasons to go beyond the one-band picture to study the original three-band model directly. For instance, (a) some important physics may be lost in the reduction to the one-band approximation (such as a role for the oxygen degrees of freedom in the pseudogap phase [8]), (b) near-degeneracies of competing states seen in the one-band case [7] may in fact be resolved with the additional degrees of freedom of the three-band model, and (c) the three-band model retains the atomic structure of the CuO_2-layer, and thus has a direct link to the structure of real materials as well as experimental measurements of orders at the atomic scale. Previously, the three-band Hubbard model has been investigated with several numerical methods, including direct simulations of finite lattices [by exact diagonalization (ED) [9–12], quantum Monte Carlo (QMC) [13–19], density matrix renormalization group (DMRG) [18, 20–22], and the random phase approximation [23–25]] and via Green's function based embedding theories [such as dynamical mean-field theory (DMFT) and its cluster extensions [26–31], and the variational cluster approximation (VCA) [32, 33]]. However, due to the complexity of the model, unlike in the one-band case, a consensus on the physics is far from reached.

Over the past few years, density matrix embedding theory (DMET) [34] has emerged as a powerful cluster embedding method. The basic idea of DMET is similar to that of (cellular) DMFT in the sense that they both map an infinite lattice to an impurity model with an environment that can be described by bath degrees of freedom, and the impurity model is self-consistently improved by matching physical quantities between a single-particle lattice solution and the correlated cluster (impurity) calculation. Technically, however, DMET has a different structure to Green's function based embedding methods, and is formulated without frequency dependence and with a finite set of bath orbitals (bounded by the number of impurity orbitals). The lack of frequency-dependent quantities means that DMET calculations can utilize efficient ground-state impurity solvers that can typically treat larger clusters than can be addressed by solvers that target the impurity Green's function. DMET has been applied to a wide range of fermionic lattice models [7, 34–38], *ab initio* chemical Hamiltonians [39–44], and non-fermionic systems [45, 46], as well as excited states [47, 48] and time-dependent problems [49]. For a detailed review of DMET, we refer to Ref. [40]. In earlier work, DMET successfully provided an accurate description of the ground-state orders of the one-band Hubbard model [36], including in the difficult underdoped region [7]. In this work, we therefore investigate the three-band Hubbard model using DMET to provide a detailed description of the ground-state phases and orders as a function of doping, with the range of parametrizations of the model that are commonly discussed in the literature.

The remaining sections of the paper are organized as follows. In Sec. II, we first present the three-band model parameters

* gkc1000@gmail.com

used in this work, and then briefly discuss the computational procedure of DMET, providing some important details for improving the robustness of the DMET algorithm. In Sec. IV, we first discuss the convergence of the DMET algorithm, followed by results for the undoped model. We then present a systematic investigation of the doped models, including characterizing the various local orders across the copper and oxygen atoms, as a function of the different literature parametrizations of the model. Sec. V summarizes the main findings of this work.

II. MODELS AND METHODS

A. Model parametrization

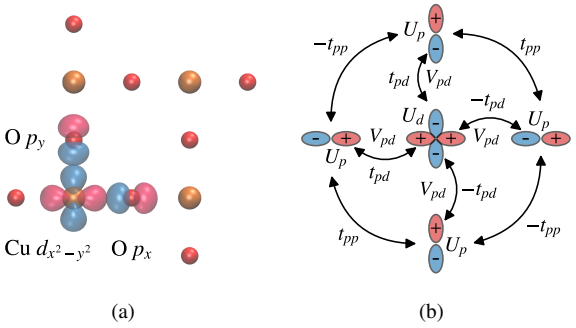

(a) (b)

FIG. 1. An illustration of the three-band Hubbard model: (a) the symmetric cluster used in the DMET calculations, where the orange and red atoms denote copper and oxygen respectively; (b) definition of the model parameters and the phase convention.

As a minimal atomic model of the CuO_2 layer in cuprates, the three-band model describes the on-site and nearest-neighbor interactions among the Cu $d_{x^2-y^2}$ and O p_x, p_y orbitals [see Fig. 1(a)]. In the hole representation, the Hamiltonian reads,

$$\begin{aligned}\mathcal{H} = & t_{pd} \sum_{\sigma \langle ij \rangle} \left(d^\dagger_{i\sigma} p_{j\sigma} + h.c. \right) + t_{pp} \sum_{\sigma \langle jj' \rangle} \left(p^\dagger_{j\sigma} p_{j'\sigma} + h.c. \right) \\ & - \Delta_{pd} \sum_{\sigma i} n^d_{i\sigma} + U_d \sum_i n^d_{i\alpha} n^d_{i\beta} + U_p \sum_j n^p_{j\alpha} n^p_{j\beta} \\ & + V_{pd} \sum_{\sigma\sigma' \langle ij \rangle} n^d_{i\sigma} n^p_{j\sigma'},\end{aligned} \tag{1}$$

where $\langle \cdots \rangle$ denotes nearest neighbors, $d^{(\dagger)}_{i\sigma}$ and $p^{(\dagger)}_{j\sigma}$ destroy (create) a hole with spin σ on the Cu d and O p orbitals respectively, $n^d_{i\sigma}$ and $n^p_{j\sigma}$ are the corresponding hole particle-number operators, and the charge transfer gap Δ_{pd} is defined as the orbital energy difference, $\epsilon_p - \epsilon_d$. Similarly to in the one-band Hubbard model, the hopping term and on-site Coulomb repulsion will be denoted t and U, and the Coulomb interaction between nearest-neighbor p, d orbitals will be denoted V_{pd}. Note that the hopping term involves a phase factor (± 1) introduced by the choice of orbital orientation in the basis as shown in Fig. 1(b).

There has been much work to determine the parameters of the three-band model; however, a consensus set does not exist [28, 50–53]. There has been particular debate about the size of the charge transfer gap Δ_{pd} [28, 54].

TABLE I. Parameters of the three-band Hubbard model used in this work, in units of eV. The parameters correspond to the hole representation.

Model	t_{pd}	Δ_{pd}	U_d	t_{pp}	U_p	V_{pd}
Hybertsen[a]	1.3	3.6	10.5			
Martin[b]	1.8	5.4	16.5			
Hanke[c]	1.5	4.5	12.0			
Hanke full[c]	1.5	4.5	12.0	0.75	5.25	0.75

[a] from Ref. [50].
[b] from Ref. [52].
[c] from Ref. [33].

In this work, we consider four sets of model parameters, see Table I. Note that all parameter sets are given in eV, thus all energies in this work are reported in units of eV unless otherwise specified. The first three sets include only the most essential terms, i.e. t_{pd}, U_d and Δ_{pd}, thus we refer to them as *minimal* parametrizations. When normalized to units of t_{pd}, the other parameters vary within a range of 10%. The fourth set involves all terms in Eq. (1). We refer to this as a *full* parametrization.

B. Computational methods

Framework. DMET approximates the expectation values in the interacting lattice by those in a quantum impurity model. The impurity model is solved simultaneously with a fictitious non-interacting lattice problem, whose ground state defines the bath sites of the impurity model via a Schmidt decomposition [34, 55]. Self-consistency is achieved by matching the one-particle density matrix of the impurity model and non-interacting lattice ground states via a *correlation potential* u applied to the non-interacting lattice. The basic steps of the DMET self-consistency loop are thus (a) compute the ground state of the non-interacting lattice Hamiltonian with correlation potential u, (b) construct the bath sites and impurity model Hamiltonian, (c) solve for the ground state of the impurity model, and (d) match the one-particle density matrices of the lattice Hamiltonian and impurity model to update u. The cycle ends when the correlation potential u is converged.

In this work, we are interested in both magnetic and superconducting phases. Consequently, the correlation potential takes the form

$$u = \sum_{ij\sigma} v^\sigma_{ij} a^\dagger_{i\sigma} a_{j\sigma} + \sum_{ij} \Delta^{\alpha\beta}_{ij} a^\dagger_{i\alpha} a^\dagger_{j\beta} + h.c., \tag{2}$$

where optimizing over v^σ and $\Delta^{\alpha\beta}$ in the self-consistency procedure allows for formation of spin polarized and singlet superconducting pairing order in the lattice and impurity problems.

The non-interacting lattice Hamiltonian is then of Bogoliubov-de Gennes form [56]. The corresponding ground-state solution is a mean-field Bardeen-Cooper-Schrieffer (BCS) wavefunction, and a set of bath orbitals that describes the environment can be constructed from the corresponding generalized density matrix. The detailed formulae for bath construction and integral transformation for the BCS mean-field can be found in Refs. [36, 57], and have been implemented in libDMET [58].

Impurity and lattice. We used a 2×2 impurity cluster [33] which retains the inversion and 4-fold rotation symmetry of the lattice [see Fig 1(a)]. We embedded the cluster in a 20×20 unit-cell (40×40 sites) lattice. We performed DMET calculations for dopings between 0.0 and 0.6. Unless otherwise specified, we initialized u with an antiferromagnetic guess and a random pairing potential.

Impurity Hamiltonian and solver. The impurity model Hamiltonian was constructed using the non-interacting DMET bath formalism [34, 36], and the ground state was determined using a density matrix renormalization group (DMRG) solver [59, 60], allowing for particle number symmetry breaking and spin polarization [36]. During the DMET self-consistent cycle we used a maximum bond dimension $M = 800$. Subsequent bond dimension convergence checks were performed using (up to) $M = 2000$. To minimize entanglement and ensure a small bond dimension M in the ground state, we rotated the impurity Hamiltonian into a basis of split-localized molecular orbitals (MOs) from the self-consistent Hartree-Fock-Bogoliubov method, where the occupied and virtual MOs were computed using the PySCF package [61], and the occupied and virtual spaces were subsequently localized separately using the Edmiston-Ruedenberg procedure that maximizes the Coulomb energy of each orbital [62, 63]. The standard genetic algorithm implemented in the Block program [63–66] was used to order the orbitals for the DMRG calculation. The tolerance of the DMRG sweep energy was set to 10^{-6}.

DMET self-consistency. We carried out DMET self-consistency using the full impurity-bath fitting [36, 40], where the cost function measures the least-squares difference between the correlated one-particle density matrix γ^{corr} and the non-interacting lattice density matrix projected to the full impurity problem γ^{mf},

$$w(u) = \sum_{kl}^{\mathrm{imp+bath}} \left[\gamma^{\mathrm{mf}}_{kl}(u) - \gamma^{\mathrm{corr}}_{kl}\right]^2. \tag{3}$$

We minimized w using a conjugate gradient (CG) minimizer with line search. Since the gap of the non-interacting lattice model is often small (in the case of doped systems) a finite inverse temperature $\beta = 1000\, t_{pd}$ was used to define the non-interacting density matrix to ensure smooth convergence (see Appendix for further discussion and expressions for the analytic gradient of the cost function at finite temperature). We matched the particle number on the impurity sites and on the lattice exactly by separately fitting the chemical potential using quadratic interpolation [57]. We employed direct inversion in the iterative subspace (DIIS) [67, 68] to accelerate the overall DMET convergence, using the difference of u between two adjacent iterations as the error vector. We chose the convergence threshold to be 10^{-4} in the correlation potential u (per site), which we observed to translate to an energy convergence per site of better than 10^{-4}.

Order parameters. To characterize the doping dependence of the ground-state, we define the average AF and d-wave SC order parameters. As usual, the AF order parameter is chosen as the staggered magnetization,

$$m_{\mathrm{AF}} = \frac{1}{4}\sum_{i\in\mathrm{Cu}} \eta^{\mathrm{AF}}_i m^d_i, \tag{4}$$

where m^d_i is the local magnetic moment on a Cu-d orbital, $\frac{1}{2}\left(n^d_{i\alpha} - n^d_{i\beta}\right)$, and the η^{AF} is the local structure factor,

$$\eta^{\mathrm{AF}}_i = \begin{cases} +1, \text{ if } n^d_{i\alpha} \geqslant n^d_{i\beta}, \\ -1, \text{ if } n^d_{i\alpha} < n^d_{i\beta}. \end{cases} \tag{5}$$

The SC order parameter here is evaluated as the average of the Cu-Cu and O-O d-wave pairing components,

$$\begin{aligned} m_{\mathrm{SC}} = &\frac{1}{4}\sum_{\langle ii'\rangle}\frac{1}{\sqrt{2}}\eta^{\mathrm{SC}}_{ii'}\left(\left\langle d_{i\alpha}d_{i'\beta}\right\rangle + \left\langle d_{i'\alpha}d_{i\beta}\right\rangle\right) \\ &+ \frac{1}{4}\sum_{\langle\langle jj'\rangle\rangle}\frac{1}{\sqrt{2}}\eta^{\mathrm{SC}}_{jj'}\left(\left\langle p_{j\alpha}p_{j'\beta}\right\rangle + \left\langle p_{j'\alpha}p_{j\beta}\right\rangle\right), \end{aligned} \tag{6}$$

where $\langle\cdots\rangle$ limits the summation such that only the pairing between nearest Cu-d orbitals is taken into account, and similarly $\langle\langle\cdots\rangle\rangle$ involves only the next-nearest coupling between O-p orbitals. The factor $\frac{1}{4}$ scales the result to one unit cell. The d-wave superconducting structure factor η^{SC} is defined as,

$$\eta^{\mathrm{SC}}_{ii'} = \begin{cases} +1, \text{ if } \mathbf{R}_i - \mathbf{R}_{i'} = \pm\mathbf{e}_x, \\ -1, \text{ if } \mathbf{R}_i - \mathbf{R}_{i'} = \pm\mathbf{e}_y. \end{cases} \tag{7}$$

III. NUMERICAL CONVERGENCE

We first assess the accuracy and convergence of the DMET procedure in the three-band model calculations. The error in the DMET calculations arises from three possible sources: (a) DMET self-consistency error (from incomplete convergence), (b) DMRG solver error due to the finite bond dimension, and (c) error from the finite size of the impurity. The finite size error (c) can, in principle, be eliminated by increasing the cluster size and extrapolating to the thermodynamic limit (TDL), as performed in the one-band Hubbard model case [36]. In this work, we use a fixed 2×2 cluster size due to the increased computational cost of the three-band model, thus we cannot assess the finite-size error. However, the error due to (a) and (b) can be estimated in our framework, which we now discuss.

Fig. 2 shows the overall convergence of DMET with respect to the number of DMET self-consistent iterations. We observe qualitatively different convergence in the normal and superconducting parts of the DMET phase diagram. To illustrate this, we plot the DMET energy, AF, and (d-wave) SC

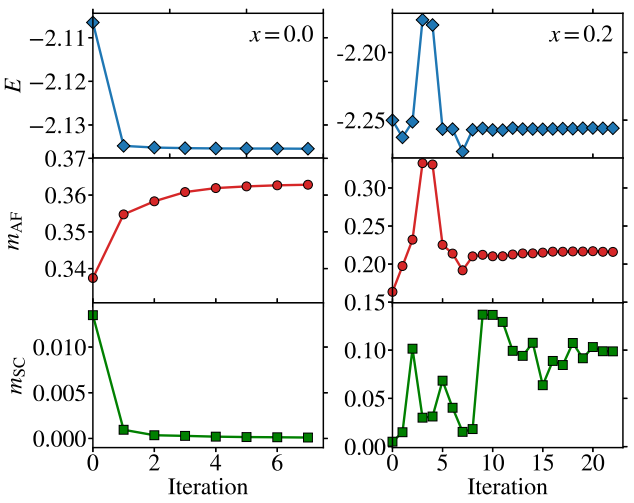

FIG. 2. DMET energy (in units of t_{pd}) and order parameters of the Hybertsen minimal parametrized three-band model, with respect to the number of iterations, at doping $x = 0.0$ (left) and $x = 0.2$ (right).

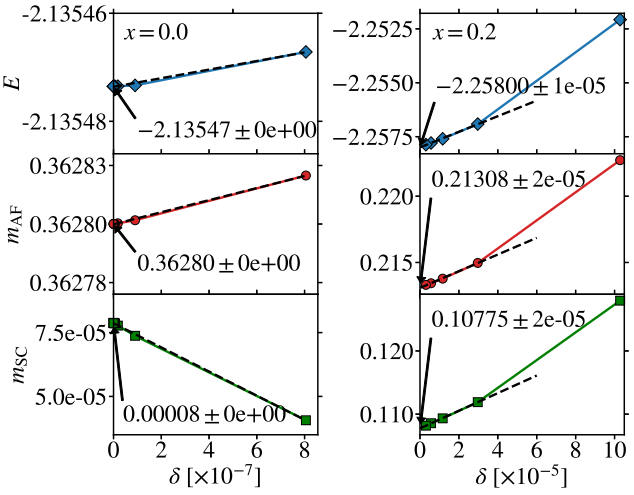

FIG. 3. DMET energy (in units of t_{pd}) and order parameters of the Hybertsen minimal parametrized three-band model, with respect to the discarded weight δ of the DMRG solver, at doping $x = 0.0$ (left) and $x = 0.2$ (right). The values are linearly extrapolated to the limit where $\delta = 0.0$ (dash line). The error shown is the standard deviation of linear regression.

order parameter for the Hybertsen model at different dopings x. (These order parameters are defined precisely in Sec. IV B). We first discuss the undoped system. Here we see that the DMET cycle converges smoothly within 7 iterations. For the DMET energy, a single DMET step is enough to converge to $\sim 10^{-4}$, demonstrating the utility of single-shot DMET calculations in normal (and especially non-magnetic) states. The order parameters (density matrices) are more strongly affected by self-consistency. We find that the AF order increases during the iterations, while the SC order is suppressed, giving a pure antiferromagnetic state at convergence. We next consider $x = 0.2$ doping. Here, the self-consistency cycle converges more slowly, requiring about 20 DMET iterations to reach convergence. The total energy as well as AF order converges at around the 10^{th} iteration, while the SC order oscillates until the 20^{th} iteration. This in part reflects the influence of the initial guess: the AF guess [v^{σ} in Eq. (2)] is quite close to the converged potential, while the SC guess [$\Delta^{\alpha\beta}$ in Eq. (2)] is initialized randomly and thus needs more iterations to converge. If we were to restrict the DMET optimization to only pairing potentials with d-wave symmetry (as is commonly done in most cluster DMFT [69] or VCA calculations [33]), the convergence would be much faster. However, the more general form of the correlation potential in DMET allows for the possibility of other pairing channels and orders to emerge, as we will see in the discussion below. The remaining DMET self-consistency error can be estimated from the difference between the expectation values (e.g. DMET energy) of the last two iterations [36], e.g. $\delta E = \frac{1}{2}|E(n-1) - E(n)|$. Consistent with our chosen convergence criterion, the typical size of the DMET self-consistency error in the undoped region is less than 10^{-5} (for both the energy and order parameters), and less than 10^{-4} (for the energy) and $\sim 10^{-3}$ (for the order parameters) in the doped region.

The error from the DMRG solver can be estimated using standard techniques based on the discarded weight in the DMRG calculation [63, 70, 71] and can be further reduced by extrapolation. The error in the impurity observables (used to evaluate the DMET energy and order parameters) is linear in the (sufficiently small) discarded weight δ and hence can be extrapolated to the exact result ($\delta = 0$) [71]. The convergence with bond dimension M for fixed correlation potential u is shown in Fig. 3. We find that the discarded weight in the normal state (undoped model) is extremely small and usually less than 10^{-8}, thus extrapolation is unnecessary. In fact, calculations can be carried out using a bond dimension as small as $M = 100$ without any significant error. On the other hand, when the system becomes superconducting, the discarded weight also increases, e.g. to 3×10^{-5} at $M = 800$, indicating that the system is more entangled. In such situations, extrapolation has a significant effect on the DMET expectation values. Compared to the extrapolated values, at $M = 800$ the error in the energy (per site) and order parameters is about 10^{-3}.

In summary, from the above analysis, we find that the DMET calculations can be smoothly converged, with minimal error from either the self-consistency or from the solver. We now proceed to discussing the physical results.

IV. THE THREE-BAND PHASE DIAGRAM

A. Undoped state

We present the order parameters for the undoped state from DMET and from reference calculations and experimental measurements in Table II. As expected, the d orbitals are roughly half-filled and the p orbitals are doubly occupied, with some charge transfer between the two due to hybridization. Notably,

TABLE II. Charge, spin distribution (magnetic moments) and energy gap of the undoped three-band Hubbard model and reference data. Note that the experimental gaps reported are all optical gaps.

Model	ρ_{Cu}	ρ_O	m_{Cu}	m_O	E_g [eV]
Hybertsen	1.238	1.881	0.363	0.000	2.5
Martin	1.219	1.891	0.375	0.001	4.4
Hanke	1.220	1.890	0.373	0.000	3.9
Hanke full	1.358	1.821	0.279	0.002	2.2
Others	1.23[a]	1.89[a]	0.29[b], 0.31[c]		2.25[b],
Cuprate			0.3 ± 0.025[d]		1.5-2.0[e], 1.5-1.7[f]

[a] DMRG result from Ref. [22], using a similar model to Hanke full (with a different $U_p = 4.5$, $V_{pd} = 1.5$ and $V_{pp} = 1.125$).
[b] VCA result from Ref. [32], using basically the same model as Hanke full (with a different $U_p = 4.5$).
[c] VCA result from Ref. [33], using the same model as Hanke full.
[d] Experimental result for La_2CuO_4, from Ref. [72].
[e] Experimental result for La_2CuO_4, from Ref. [73–75].
[f] Experimental result for $YBa_2Cu_3O_6$, from Ref. [74, 76].

in the full parametrization, the Cu site is more strongly occupied by electrons, due to the inclusion of the U_p term which introduces an energy penalty for double occupancy on the O site. Unlike on the O site, the spin density on the Cu site is polarized, with a strong local magnetic moment, comparable to the experimental value 0.3 ± 0.025 ($0.6 \pm 0.05\ \mu_B$) [72], as well as the theoretical results of 0.29 [32] and 0.31 [32] from VCA. In addition, the magnetic moment in the full parametrization is reduced, because the increase in electron density on the copper dilutes the polarized spin, while the additional holes on oxygen reduce the super-exchange antiferromagnetic coupling. We note that the local magnetic moment in the minimal models appears to be slightly too large, while that of the full model more closely matches experiment.

As a simple estimate of the single-particle gap, we also computed the energy gap of the converged DMET non-interacting lattice Hamiltonian (DMET NI gap), i.e. $E_g = \varepsilon_{CBM} - \varepsilon_{VBM}$, where C(V)BM denotes conduction (valence) band minimum (maximum). Note that although the charge and spin densities in the different parametrizations are generally similar, the DMET NI gap varies significantly, from 2.2 to 4.4 eV. The Hybertsen and Hanke parameter sets were derived from calculations on La_2CuO_4 (LCO), where the optical energy gap is variously reported as lying in the range 1.5 to 2.0 eV [73–75] (Note that the optical gap is generally smaller than the fundamental gap). The estimated DMET NI gap of 2.5 eV and 2.2 eV for the Hybertsen and Hanke full parameter set respectively are thus in reasonable agreement with the experimental gap. However, the minimal Hanke parametrization seriously overestimates the gap. The Martin parameter set, obtained from calculations on finite-sized Cu-O clusters, are all systematically larger than in the other sets, and thus give the largest DMET NI gap. However, since the ratio of parameters in the Martin model remains similar to other parametrizations (and thus give rise to similar charge and spin distributions) this suggests that all energy parameters in the Martin model should simply be simultaneously rescaled downwards.

In Fig. 4(a), we plot the electronic band structure and projected density of states (PDOS) from the DMET non-interacting lattice Hamiltonian, as converged for the fully parametrized Hanke model. The CBM is mainly of Cu d character (upper Hubbard band), while the VBM shows mixed character with slightly more O-p. The mixed orbital character of the valence bands around the Fermi level is consistent with the Zhang-Rice singlet (ZRS) hypothesis [4], in which hybridization between oxygen and copper orbitals induces superexchange that leads to singlets of O and Cu holes. Also, we find that the weight of Cu-d is greater at the Γ point, while that of O-p is larger at the M point, consistent with model analysis of the ZRS state [77] and results from VCA [32]. These observations indicate that the undoped three-band model ground state is a charge transfer insulator, with mainly a p-d type energy gap (see also Ref. [78] for experimental evidence of the charge-transfer nature of the band gap). We find significant d-p hybridization across the whole energy window, even for "core" oxygen bands. This illustrates the challenges in finding a simple downfolding of the 3-band model to the 1-band model.

Finally, to show the effect of correlations introduced by DMET on the spectrum, we also plot the band structure from a self-consistent Hartree-Fock (HF) calculation in Fig. 4(b). In the HF mean-field description, the band gap ($\sim$ 3 eV) is much larger than in DMET, and the d-p hybridization is much weaker, resulting in a VBM with dominant oxygen p character. Overall, the band structure from the DMET lattice mean-field shows greater hybridization and a more reasonable band gap value as a result of electron correlations.

B. Doped states

More interesting ground states, including those with superconducting order, appear under doping. Although our calculations are all at zero temperature, we can loosely identify an observed large order parameter to a large transition temperature in the phase diagram, thus allowing for an experimental consistency check on our observed results. In Fig. 5, we plot the AF and d-wave SC order parameters as a function of hole doping. In the fully parametrized model, we show two different solutions of the DMET self-consistency, labelled solution 1 (obtained starting from a strongly spin polarized AF guess) and solution 2 (obtained starting from a weakly polarized AF guess).

For all parameter sets, we observe that the AF order parameter decreases as doping increases, consistent with the general behavior of the cuprate phase diagram [78]. However, for the minimal models, the AF order persists even up to large dopings (e.g. ~ 0.15 at $x = 0.3$). In principle, this unphysical behavior could originate either from the remaining finite size error in the DMET calculation, or from the unphysical nature of the parametrization. From our earlier work on the 1-band Hubbard model [36], we observe that DMET calculations using a 2×2 impurity (e.g. in the range $U/t = 6 - 8$) do indeed show an overpolarization of the spin (see Fig. 1 of the Supplemental Material [79]). However, the AF order nonetheless vanishes at dopings larger than 0.25, more rapidly

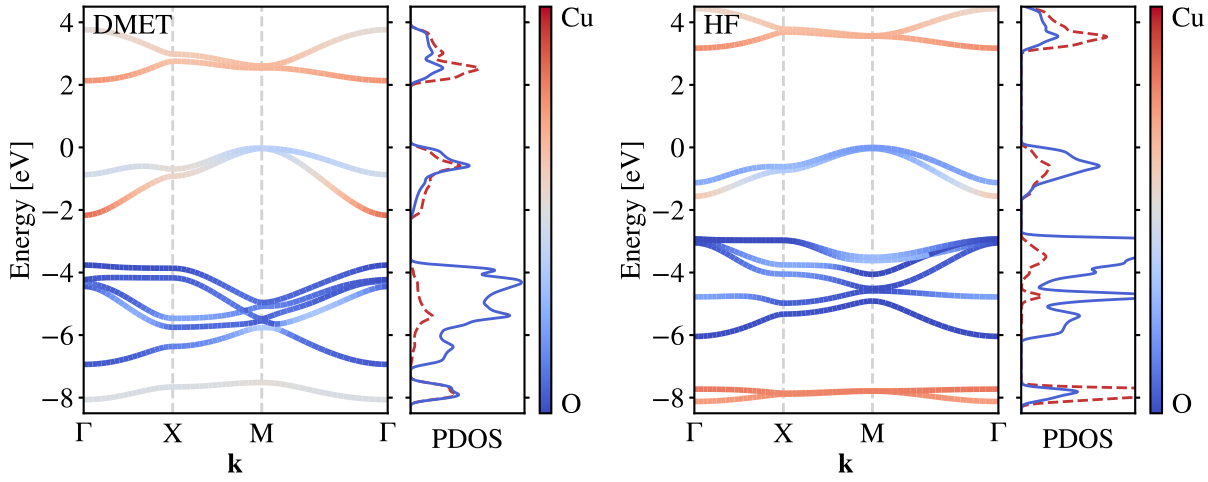

FIG. 4. Orbital-projected electronic band structure and density of states (PDOS) of the undoped three-band Hubbard model with Hanke full parameters from DMET (left) and HF (right). The special **k** points [Γ: $(0,0)$, X: $(\pi,0)$, M: (π,π)] are in the first Brillouin zone of the 2×2 supercell lattice. The valence band maximum (VBM) is chosen as the energy zero.

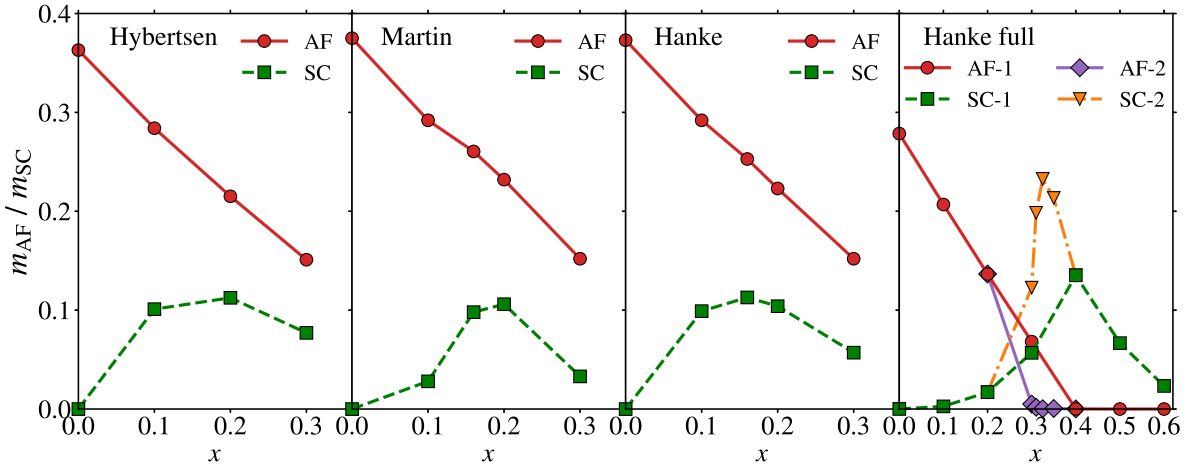

FIG. 5. Antiferromagnetic and d-wave superconducting order parameter of the hole-doped three-band Hubbard model. The model settings are from Hybertsen, Martin, Hanke minimal and Hanke full parameter sets (from left to right). Note that in the "Hanke full" case, we find two possible solutions between $x = 0.2$ and $x = 0.4$, marked as solution "1" (from a strongly polarized AF guess) and "2" (from a weakly polarized AF guess) in the figure.

than what we observe in the minimal parametrized three-band model. Also, the full parametrization of the 3-band model also predicts a more realistic trend for the AF order at large doping. Taken together, this suggests that the persistent AF order we observe under doping is likely due to the oversimplified minimal model parameters. We note that although the AF order in the full model does decrease to zero in the observed doping range, it vanishes between $x = 0.2$ and 0.3. This is beyond the experimental boundary for the pure AF phase ($x < 0.1$), but close to the boundary of the pseudogap region [80, 81].

From Fig. 5, we see that the d-wave superconducting order (coexisting with antiferromagnetism) appears in the phase diagram of all parameter sets. In the minimal models, the d-wave pairing reaches a maximum at around $x = 0.15-0.20$. Due to the overestimation of AF order discussed above, the minimal models show coexistence of AF + SC order for all the studied dopings. However, in the full parametrization, the two coexist in the range 0.1 to 0.4 (for solution 1), and 0.1 to 0.3 (for solution 2), with d-wave order reaching a maximum near $x \sim 0.30 - 0.35$, somewhat larger than seen in experiments ($\sim$ 0.15 - 0.2) [72]. Solutions 1 and 2 coincide for $x < 0.2$ and $x > 0.4$ but are distinct in between, reflecting the known competition between orders at intermediate doping [81]; solution 2 is slightly lower in energy and displays significantly

stronger superconducting order. Note that it is also possible to converge a paramagnetic SC solution (by constraining the correlation potential i.e. $v^\alpha = v^\beta$ and $\Delta = \Delta^\dagger$). In this case, the SC order is already evident at $x = 0.1$, since the AF order is artificially suppressed. However, the energy of this paramagnetic state is much higher than the AF + SC states we have discussed, and is unstable if one releases the constraints on the potential. We thus believe the coexistence of AF and SC order to be a true feature of the 3-band model ground state, as has also been observed in VCA studies [32, 33].

Beyond the bulk order parameters, the 3-band model and the explicit inclusion of both copper and oxygen atoms into the DMET impurity cluster allows for the possibility of studying the magnetic and superconducting order at the atomic scale. The explicit charge, spin, and pairing orders are shown in Fig. 6. We only present representative results from the Hanke full model at $x = 0.0$ and $x = 0.3$ (solution 2) doping, since results from other parametrizations and dopings are qualitatively similar. (further plots are presented in the Supplemental Material [79]). Comparing Fig. 6(a) and Fig. 6(b), we see that on doping the holes mainly occupy the oxygen sites and the hole density on copper only increases slightly. Combined with the fact that doped electrons mainly reside on Cu (not shown) this reflects the particle-hole asymmetry of the three-band model [22, 81]. With respect to pairing order, we see $d_{x^2-y^2}$-wave symmetry clearly between neighboring Cu sites (i.e. it transforms according to the B-representation of the C_4 group and the sign of the pairing changes on rotating by 90°), see Fig. 6(b). The Cu-Cu pairing order is the largest pairing order between the atoms. From Fig. 6(c), we also see d-wave order between the *next-nearest* O p orbitals. Although the magnitude is slightly smaller than that of the Cu-Cu pairing, it still contributes almost $\sim 50\%$ of the bulk d-wave order in Eq. (6). Finally, we consider the pairing order between Cu-O and the nearest O-O atoms, see Fig. 6(d). We see that the coupling between the nearest O-O atoms has s-wave symmetry but is quite weak, related to the incompatible orbital orientations. On the other hand, we find the pairing between Cu-O to be relatively strong (in all parameter sets). The local symmetry of Cu-O coupling has $p_{x(y)}$-wave [or $d_{xy(yz)}$-wave] symmetry (the pattern transforms according to the E-representation of the C_4 group), which to our knowledge has not previously been reported. This points to the possibility of microscopic inhomogeneities on the atomic scale.

V. CONCLUSIONS

In summary, we have applied density matrix embedding theory to characterize the ground-states of the three-band Hubbard model in four parametrizations. Our error estimates show that the DMET solutions can be numerically tightly converged. We have calculated the charge, local magnetic moments, projected energy bands and density of states of the undoped three-band model, which support a charge-transfer insulating character at zero doping. We also studied the doping dependence of the ground-state (phase diagram) of the model paying particular attention to the local antiferromagnetic (AF) and superconducting (SC) orders. All four parameter sets find a decrease in AF order upon doping and a SC dome. The minimal models all predict coexistence of AF + SC orders, while the full model finds a region of either AF + SC coexistence or a pure SC order depending on the self-consistent solution. Comparison to experimental data and earlier theoretical studies suggests that the minimal parametrized models overestimate the AF order and lead to poorer energy gaps, relative to the full parametrizations, which also include oxygen and oxygen-copper Coulomb repulsion, and oxygen-oxygen hopping. These additional terms of the full parametrization thus appear important for quantitative accuracy in the three-band model. There remain some quantitative differences, however, between the observed doping dependence of the AF and SC orders in the full parametrization and that of real materials, and more work is required to understand whether such differences arise from the numerical approximations of cluster size or the model parameters themselves. In the SC region, we observe strong d-wave pairing between Cu-Cu and the next-nearest O-O, weak extended s-wave coupling between the nearest O-O atoms, and p- (or d_{xz}, d_{yz})-like symmetry pairing between Cu-O. The latter order illustrates the detailed physics that emerges at atomic length-scales in the three-band model, and the potential for new and more complicated phases to emerge. Exploring such questions will be the subject of future work.

ACKNOWLEDGMENTS

We thank Alec White, Nai-Chang Yeh, Patrick Lee, Tianyu Zhu and Yang Gao for helpful discussions. This work was supported by the US Department of Energy, Office of Science, via award No. 19390. GKC is a Simons Investigator in Physics.

Appendix: Analytic gradients of cost function Eq. (3) at finite temperature

Once the gradients of Eq. (3) are obtained, we can utilize efficient gradient-based numerical methods, such as CG or the Broyden-Fletcher-Goldfarb-Shanno (BFGS) algorithm, to optimize the correlation potential. By differentiating Eq. (3) with respect to u_{ij} we have,

$$\frac{\partial w}{\partial u_{ij}} = 2 \sum_{kl} \left(\gamma^{\mathrm{mf}} - \gamma^{\mathrm{corr}}\right)_{kl} \frac{\partial \gamma^{\mathrm{mf}}_{kl}}{\partial u_{ij}}, \tag{A.1}$$

and thus the key component of Eq. (A.1) is to evaluate the response of the mean-field density matrix with respect to a perturbation, $\partial \gamma^{\mathrm{mf}}_{kl} / \partial u_{ij}$. The response at zero temperature has been expressed in terms of orbital coefficients and energies in Ref. [40, 57] using first order perturbation theory,

$$\frac{\partial \gamma^{\mathrm{mf}}_{kl}}{\partial u_{ij}} = \sum_{p}^{\mathrm{occ}} \sum_{q}^{\mathrm{virt}} \frac{C_{kp} C^*_{lq} C_{iq} C^*_{jp} - C_{kq} C^*_{lp} C^*_{iq} C_{jp}}{\epsilon_p - \epsilon_q}, \tag{A.2}$$

where we have assumed the system is *gapped*. However, when the system becomes (nearly) gapless, this expression diverges.

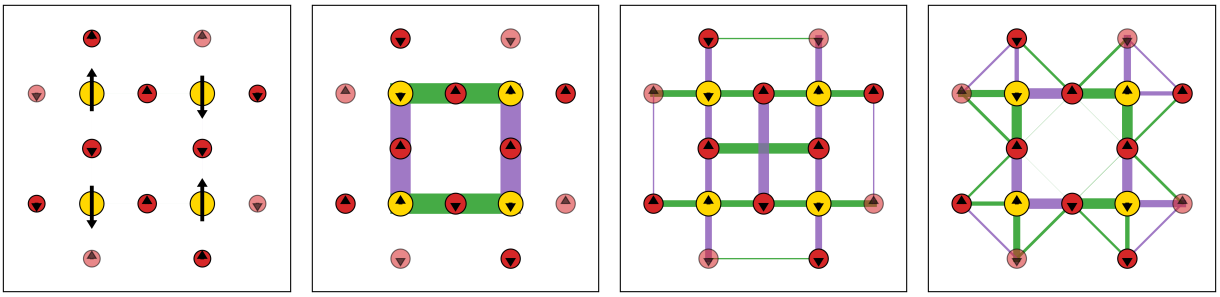

(a) $x = 0.0$ (b) $x = 0.3$, Cu-Cu (c) $x = 0.3$, next-nearest O-O (d) $x = 0.3$, Cu-O, nearest O-O

FIG. 6. Charge, spin and pairing distributions of the three-band Hubbard model. We use yellow and red circles for Cu and O respectively. The area of the circle reflects the corresponding local hole density, the length of the arrow denotes the magnitude of the local magnetic moment, the width of the ribbon is proportional to the pairing strength and different colors of the ribbon denote different signs of coupling. The results are calculated based on the fully parametrized model at $x = 0.0$ [(a)] and $x = 0.3$ doping [solution 2, (b) - (d)]. (b) shows the pairing strength between Cu and Cu; (c) shows the pairing strength between the next nearest neighbor O; (d) illustrates the coupling of both the nearest Cu-O, and the nearest O-O.

In such cases, the divergent gradient causes the optimization to fail, and this is a source of many convergence difficulties in DMET.

One strategy to solve this issue is to introduce a finite temperature smearing, similar to what is used in mean-field calculations of metals. With an inverse temperature β and a perturbation δu, the Fermi-Dirac density matrix is defined as,

$$\gamma_{kl} = \left[1 + e^{\beta(h-\mu+\delta u)}\right]^{-1}_{kl}, \tag{A.3}$$

where μ is the Fermi level for the (quasi-)particles. Note that the chemical potential term here represents the Fermi level of the Bogoliubov quasiparticles. The response of γ with respect to the correlation potential u then involves two terms,

$$\frac{d\gamma_{kl}[u,\mu(u)]}{du_{ij}} = \left.\frac{\partial\gamma_{kl}}{\partial u_{ij}}\right|_{\mu} + \frac{\partial\gamma_{kl}}{\partial\mu}\frac{\partial\mu}{\partial u_{ij}}, \tag{A.4}$$

where the first term is the direct response of the density at a fixed Fermi level, while the second term reflects the contribution of the implicit change in the Fermi level due to the change in potential. The final expression for the first term in Eq. (A.4) is,

$$\frac{\partial\gamma_{kl}}{\partial u_{ij}} = \sum_{pq} C_{kp}C^*_{ip}K_{pq}C_{jq}C^*_{lq}, \tag{A.5}$$

where

$$K_{pq} \equiv n_p(1-n_q)\frac{1-e^{\beta(\varepsilon_p-\varepsilon_q)}}{\varepsilon_p-\varepsilon_q}. \tag{A.6}$$

It is easy to check that K_{pq} is always finite when $\varepsilon_p = \varepsilon_q$. One can also let β go to infinity and choose p / q to label occupied / virtual orbitals; the gradient then gives the correct zero temperature limit in Eq. (A.2) (up to a symmetrization).

The final expressions for the second term in Eq. (A.4) are,

$$\begin{aligned}\frac{\partial\gamma_{kl}}{\partial\mu} &= \sum_p \beta C_{kp}n_p(1-n_p)C^*_{lp},\\ \frac{\partial\mu}{\partial u_{ij}} &= \left[\sum_p n_p(1-n_p)C^*_{ip}C_{jp}\right] \Big/ \left[\sum_p n_p(1-n_p)\right].\end{aligned} \tag{A.7}$$

Usually this contribution is very small at low temperatures, compared to the direct response in Eq. (A.5). However, this contribution will be important in a real finite temperature simulation, e.g. in Ref. [48].

We summarize the derivation of Eq. (A.5) - (A.7) in the Supplemental Material [79].

[1] V. J. Emery, Theory of High-T_c Superconductivity in Oxides, Phys. Rev. Lett. **58**, 2794 (1987).

[2] J. Hubbard, Electron correlations in narrow energy bands, Proc. R. Soc. London A **276**, 238 (1963).

[3] P. W. Anderson, The Resonating Valence Bond State in La_2CuO_4 and Superconductivity, Science **235**, 1196 (1987).

[4] F. C. Zhang and T. M. Rice, Effective Hamiltonian for the superconducting Cu oxides, Phys. Rev. B **37**, 3759 (1988).

[5] H. Sakakibara, H. Usui, K. Kuroki, R. Arita, and H. Aoki, Two-Orbital Model Explains the Higher Transition Temperature of the Single-Layer Hg-Cuprate Superconductor Compared to That of the La-Cuprate Superconductor, Phys. Rev. Lett. **105**, 057003 (2010).

[6] J. LeBlanc, A. E. Antipov, F. Becca, I. W. Bulik, G. K.-L. Chan, C.-M. Chung, Y. Deng, M. Ferrero, T. M. Henderson, C. A. Jiménez-Hoyos, E. Kozik, X.-W. Liu, A. J. Millis, N. ProkofâĂŹev, M. Qin, G. E. Scuseria, H. Shi, B. Svistunov, L. F. Tocchio, I. Tupitsyn, S. R. White, S. Zhang, B.-X. Zheng, Z. Zhu, and E. Gull, Solutions of the Two-Dimensional Hubbard Model: Benchmarks and Results from a Wide Range of

Numerical Algorithms, Phys. Rev. X **5**, 041041 (2015).
[7] B.-X. Zheng, C.-M. Chung, P. Corboz, G. Ehlers, M.-P. Qin, R. M. Noack, H. Shi, S. R. White, S. Zhang, and G. K.-L. Chan, Stripe order in the underdoped region of the two-dimensional Hubbard model, Science **358**, 1155 (2017).
[8] B. Fauqué, Y. Sidis, V. Hinkov, S. Pailhès, C. T. Lin, X. Chaud, and P. Bourges, Magnetic Order in the Pseudogap Phase of High T_c Superconductors, Phys. Rev. Lett. **96**, 197001 (2006).
[9] M. S. Hybertsen, E. B. Stechel, M. Schluter, and D. R. Jennison, Renormalization from density-functional theory to strong-coupling models for electronic states in Cu-O materials, Phys. Rev. B **41**, 11068 (1990).
[10] R. T. Scalettar, D. J. Scalapino, R. L. Sugar, and S. R. White, Antiferromagnetic, charge-transfer, and pairing correlations in the three-band Hubbard model, Phys. Rev. B **44**, 770 (1991).
[11] M. Cini and A. Balzarotti, Cluster approach to the three-band Hubbard model of the Cu-O plane: Superconducting pairs, Phys. Rev. B **56**, 14711 (1997).
[12] T. Shirakawa, H. Watanabe, and S. Yunoki, Theoretical Studies of a Three-band Hubbard Model with a Strong Spin-orbit Coupling for 5d Transition Metal Oxide Sr_2IrO_4, J. Phys.: Conf. Ser. **454**, 012068 (2013).
[13] G. Dopf, A. Muramatsu, and W. Hanke, Three-band Hubbard model: A Monte Carlo study, Phys. Rev. B **41**, 9264 (1990).
[14] K. Kuroki and H. Aoki, Quantum Monte Carlo Evidence for Superconductivity in the Three-Band Hubbard Model in Two Dimensions, Phys. Rev. Lett. **76**, 4400 (1996).
[15] M. Guerrero, J. E. Gubernatis, and S. Zhang, Quantum Monte Carlo study of hole binding and pairing correlations in the three-band Hubbard model, Phys. Rev. B **57**, 11980 (1998).
[16] T. Yanagisawa, S. Koike, and K. Yamaji, Ground state of the three-band Hubbard model, Phys. Rev. B **64**, 184509 (2001).
[17] Y. F. Kung, C.-C. Chen, Y. Wang, E. W. Huang, E. A. Nowadnick, B. Moritz, R. T. Scalettar, S. Johnston, and T. P. Devereaux, Characterizing the three-orbital Hubbard model with determinant quantum Monte Carlo, Phys. Rev. B **93**, 155166 (2016).
[18] E. W. Huang, C. B. Mendl, S. Liu, S. Johnston, H.-C. Jiang, B. Moritz, and T. P. Devereaux, Numerical evidence of fluctuating stripes in the normal state of high-T_c cuprate superconductors, Science **358**, 1161 (2017).
[19] E. Vitali, H. Shi, A. Chiciak, and S. Zhang, Metal-insulator transition in the ground state of the three-band hubbard model at half filling, Phys. Rev. B **99**, 165116 (2019).
[20] E. Jeckelmann, D. J. Scalapino, and S. R. White, Comparison of different ladder models, Phys. Rev. B **58**, 9492 (1998).
[21] S. Nishimoto, E. Jeckelmann, and D. J. Scalapino, Differences between hole and electron doping of a two-leg CuO ladder, Phys. Rev. B **66**, 245109 (2002).
[22] S. R. White and D. J. Scalapino, Doping Asymmetry and Striping in a Three-orbital CuO_2 Hubbard Model, Phys. Rev. B **92**, 205112 (2015).
[23] S. Bulut, W. A. Atkinson, and A. P. Kampf, Spatially modulated electronic nematicity in the three-band model of cuprate superconductors, Phys. Rev. B **88**, 155132 (2013).
[24] T. A. Maier and D. J. Scalapino, Pairing Interaction Near a Nematic Quantum Critical Point of a Three-band CuO_2 model, Phys. Rev. B **90**, 174510 (2014).
[25] W. A. Atkinson, A. P. Kampf, and S. Bulut, Charge order in the pseudogap phase of cuprate superconductors, New J. Phys. **17**, 013025 (2015).
[26] T. Maier, M. Zölfl, T. Pruschke, and J. Keller, Magnetic properties of the three-band Hubbard model, Eur. Phys. J. B **7**, 377 (1999).
[27] M. Zölfl, T. Maier, T. Pruschke, and J. Keller, Electronic properties of CuO_2-planes: A DMFT study, Eur. Phys. J. B **13**, 47 (2000).
[28] P. R. C. Kent, T. Saha-Dasgupta, O. Jepsen, O. K. Andersen, A. Macridin, T. A. Maier, M. Jarrell, and T. C. Schulthess, Combined density functional and dynamical cluster quantum Monte Carlo calculations of the three-band Hubbard model for hole-doped cuprate superconductors, Phys. Rev. B **78**, 035132 (2008).
[29] L. de' Medici, X. Wang, M. Capone, and A. J. Millis, Correlation Strength, Gaps, and Particle-hole Asymmetry in High-T_c Cuprates: A Dynamical Mean Field Study of the Three-band Copper-oxide Model, Phys. Rev. B **80**, 054501 (2009).
[30] C. Weber, C. Yee, K. Haule, and G. Kotliar, Scaling of the transition temperature of hole-doped cuprate superconductors with the charge-transfer energy, EPL **100**, 37001 (2012).
[31] A. Go and A. J. Millis, Spatial Correlations and the Insulating Phase of the High T_c Cuprates: Insights from a Configuration-Interaction-Based Solver for Dynamical Mean Field Theory, Phys. Rev. Lett. **114**, 016402 (2015).
[32] E. Arrigoni, M. Aichhorn, M. Daghofer, and W. Hanke, Phase Diagram and Single-particle Spectrum of CuO_2 high-T_c Layers: Variational Cluster Approach to the Three-band Hubbard Model, New J. Phys. **11**, 055066 (2009).
[33] W. Hanke, M. Kiesel, M. Aichhorn, S. Brehm, and E. Arrigoni, The 3-band Hubbard-model versus the 1-band model for the high-T_c cuprates: Pairing dynamics, superconductivity and the ground-state phase diagram, Eur. Phys. J. Spec. Top. **188**, 15 (2010).
[34] G. Knizia and G. K.-L. Chan, Density matrix embedding: A simple alternative to dynamical mean-field theory, Phys. Rev. Lett. **109**, 186404 (2012).
[35] I. W. Bulik, G. E. Scuseria, and J. Dukelsky, Density matrix embedding from broken symmetry lattice mean fields, Phys. Rev. B **89**, 035140 (2014).
[36] B.-X. Zheng and G. K.-L. Chan, Ground-state phase diagram of the square lattice Hubbard model from density matrix embedding theory, Phys. Rev. B **93**, 035126 (2016).
[37] B.-X. Zheng, J. S. Kretchmer, H. Shi, S. Zhang, and G. K.-L. Chan, Cluster size convergence of the density matrix embedding theory and its dynamical cluster formulation: A study with an auxiliary-field quantum Monte Carlo solver, Phys. Rev. B **95**, 045103 (2017).
[38] X. Wu, Z.-H. Cui, Y. Tong, M. Lindsey, G. K.-L. Chan, and L. Lin, Projected density matrix embedding theory with applications to the two-dimensional hubbard model, J. Chem. Phys. **151**, 064108 (2019).
[39] G. Knizia and G. K.-L. Chan, Density Matrix Embedding: A Strong-Coupling Quantum Embedding Theory, J. Chem. Theory Comput. **9**, 1428 (2013).
[40] S. Wouters, C. A. Jiménez-Hoyos, Q. Sun, and G. K.-L. Chan, A Practical Guide to Density Matrix Embedding Theory in Quantum Chemistry, J. Chem. Theory Comput. **12**, 2706 (2016).
[41] H. Q. Pham, V. Bernales, and L. Gagliardi, Can Density Matrix Embedding Theory with the Complete Activate Space Self-Consistent Field Solver Describe Single and Double Bond Breaking in Molecular Systems?, J. Chem. Theory Comput. **14**, 1960 (2018).
[42] I. W. Bulik, W. Chen, and G. E. Scuseria, Electron correlation in solids via density embedding theory, J. Chem. Phys. **141**, 054113 (2014).
[43] Z.-H. Cui, T. Zhu, and G. K.-L. Chan, Efficient implementation of ab initio quantum embedding in periodic systems: Density matrix embedding theory, J. Chem. Theory Comput. (2019).
[44] H. Q. Pham, M. R. Hermes, and L. Gagliardi, Periodic electronic

structure calculations with density matrix embedding theory, J. Chem. Theory Comput. (2019).
[45] Z. Fan and Q.-l. Jie, Cluster density matrix embedding theory for quantum spin systems, Phys. Rev. B **91**, 195118 (2015).
[46] B. Sandhoefer and G. K.-L. Chan, Density matrix embedding theory for interacting electron-phonon systems, Phys. Rev. B **94**, 085115 (2016).
[47] G. H. Booth and G. K.-L. Chan, Spectral functions of strongly correlated extended systems via an exact quantum embedding, Phys. Rev. B **91**, 155107 (2015).
[48] C. Sun, U. Ray, Z.-H. Cui, M. Stoudenmire, M. Ferrero, and G. K. Chan, Finite temperature density matrix embedding theory, arXiv preprint arXiv:1911.07439 (2019).
[49] J. S. Kretchmer and G. K.-L. Chan, A real-time extension of density matrix embedding theory for non-equilibrium electron dynamics, J. Chem. Phys. **148**, 054108 (2018).
[50] M. S. Hybertsen, M. Schlüter, and N. E. Christensen, Calculation of Coulomb-interaction Parameters for La_2CuO_4 using a Constrained-density Functional Approach, Phys. Rev. B **39**, 9028 (1989).
[51] A. K. McMahan, J. F. Annett, and R. M. Martin, Cuprate parameters from numerical Wannier functions, Phys. Rev. B **42**, 6268 (1990).
[52] R. L. Martin, Electronic localization in the cuprates, Phys. Rev. B **53**, 15501 (1996).
[53] M. Hirayama, Y. Yamaji, T. Misawa, and M. Imada, Ab initio effective Hamiltonians for cuprate superconductors, Phys. Rev. B **98**, 134501 (2018).
[54] A. Chiciak, E. Vitali, H. Shi, and S. Zhang, Magnetic orders in the hole-doped three-band Hubbard model: Spin spirals, nematicity, and ferromagnetic domain walls, Phys. Rev. B **97**, 235127 (2018).
[55] I. Peschel, Special Review: Entanglement in Solvable Many-Particle Models, Braz. J. Phys. **42**, 267 (2012).
[56] P.-G. de Gennes, Superconductivity of Metals and Alloys (Benjamin, New York, 1966).
[57] B.-X. Zheng, Density Matrix Embedding Theory and Strongly Correlated Lattice Systems, arXiv: 1803.10259 [cond-mat] (2018).
[58] B.-X. Zheng, https://bitbucket.org/zhengbx/libdmet.
[59] S. R. White, Density matrix formulation for quantum renormalization groups, Phys. Rev. Lett. **69**, 2863 (1992).
[60] S. R. White, Density-matrix algorithms for quantum renormalization groups, Phys. Rev. B **48**, 10345 (1993).
[61] Q. Sun, T. C. Berkelbach, N. S. Blunt, G. H. Booth, S. Guo, Z. Li, J. Liu, J. D. McClain, E. R. Sayfutyarova, S. Sharma, S. Wouters, and G. K.-L. Chan, PySCF: the Python-based simulations of chemistry framework, WIREs Comput. Mol. Sci. **8**, e1340 (2018).
[62] C. Edmiston and K. Ruedenberg, Localized Atomic and Molecular Orbitals, Rev. Mod. Phys. **35**, 457 (1963).
[63] G. K.-L. Chan and M. Head-Gordon, Highly correlated calculations with a polynomial cost algorithm: A study of the density matrix renormalization group, J. Chem. Phys. **116**, 4462 (2002).
[64] G. K.-L. Chan, An algorithm for large scale density matrix renormalization group calculations, J. Chem. Phys. **120**, 3172 (2004).
[65] G. K.-L. Chan and S. Sharma, The Density Matrix Renormalization Group in Quantum Chemistry, Annu. Rev. Phys. Chem. **62**, 465 (2011).
[66] S. Sharma and G. K.-L. Chan, Spin-adapted density matrix renormalization group algorithms for quantum chemistry, J. Chem. Phys. **136**, 124121 (2012).
[67] P. Pulay, Convergence Acceleration of Iterative Sequences. The Case of SCF Iteration, Chem. Phys. Lett. **73**, 393 (1980).
[68] P. Pulay, Improved SCF convergence acceleration, J. Comput. Chem. **3**, 556 (1982).
[69] D. Sénéchal, An introduction to quantum cluster methods, arXiv: 0806.2690 [cond-mat] (2008).
[70] Ö. Legeza and G. Fáth, Accuracy of the density-matrix renormalization-group method, Phys. Rev. B **53**, 14349 (1996).
[71] S. R. White and A. L. Chernyshev, Néel Order in Square and Triangular Lattice Heisenberg Models, Phys. Rev. Lett. **99**, 127004 (2007).
[72] K. Yamada, E. Kudo, Y. Endoh, Y. Hidaka, M. Oda, M. Suzuki, and T. Murakami, The Effect of the Heat Treatments on the Antiferromagnetism in $La_2CuO_{4-\delta}$ Single Crystals, Solid State Commun. **64**, 753 (1987).
[73] Y. Tokura, S. Koshihara, T. Arima, H. Takagi, S. Ishibashi, T. Ido, and S. Uchida, Cu-O Network Dependence of Optical Charge-transfer Gaps and Spin-pair Excitations in Single-CuO_2-layer Compounds, Phys. Rev. B **41**, 11657 (1990).
[74] S. L. Cooper, G. Thomas, A. Millis, P. Sulewski, J. Orenstein, D. Rapkine, S.-W. Cheong, and P. Trevor, Optical studies of gap, exchange, and hopping energies in the insulating cuprates, Phys. Rev. B **42**, 10785 (1990).
[75] S. Uchida, T. Ido, H. Takagi, T. Arima, Y. Tokura, and S. Tajima, Optical Spectra of $La_{2-x}Sr_xCuO_4$: Effect of Carrier Doping on the Electronic Structure of the CuO_2 Plane, Phys. Rev. B **43**, 7942 (1991).
[76] H. Romberg, N. Nücker, J. Fink, T. Wolf, X. Xi, B. Koch, H. Geserich, M. Dürrler, W. Assmus, and B. Gegenheimer, Dielectric function of $YBa_2Cu_3O_7$ between 50 mev and 50 ev, Z. Phys., B, Condens. matter. **78**, 367 (1990).
[77] J. Jefferson, H. Eskes, and L. Feiner, Derivation of a single-band model for CuO_2 planes by a cell-perturbation method, Phys. Rev. B **45**, 7959 (1992).
[78] A. Damascelli, Z. Hussain, and Z.-X. Shen, Angle-resolved photoemission studies of the cuprate superconductors, Rev. Mod. Phys. **75**, 473 (2003).
[79] See Supplemental Material at http://link.aps.org/supplemental/xxxx for the AF order of the one-band Hubbard model, additional figures of charge, spin and pairing patterns of the three-band model and the derivation of the analytic gradient of the cost function.
[80] T. Timusk and B. Statt, The pseudogap in high-temperature superconductors: An experimental survey, Rep. Prog. Phys. **62**, 61 (1999).
[81] P. A. Lee, N. Nagaosa, and X.-G. Wen, Doping a Mott Insulator: Physics of High-Temperature Superconductivity, Rev. Mod. Phys. **78**, 17 (2006).